Petroleum Science 23 (2026) 3160–3179

Contents lists available at ScienceDirect

Petroleum Science

journal homepage: www.keaipublishing.com/en/journals/petroleum-science

Original Paper

High-fidelity numerical simulation of ocean-bottom node 4C seismic data using the acoustic-elastic coupling equation

Peng-Fei Yu [a,*], Yong-Tian Zhao [b], Jia-Wei Zhang [b], Xiao-Hui Yang [c], Chao Zhang [d,**]

[a] School of Resources and Geosciences, China University of Mining and Technology, Xuzhou, 221116, Jiangsu, China
[b] College of Oceanography, Hohai University, Nanjing, 210024, Jiangsu, China
[c] College of Civil Engineering, Xuzhou University of Technology, Xuzhou, 221018, Jiangsu, China
[d] School of Carbon Neutrality Science and Engineering, Anhui University of Science and Technology, Hefei, 231131, Anhui, China

ARTICLE INFO

Article history:
Received 14 January 2025
Received in revised form
27 October 2025
Accepted 25 December 2025
Available online 21 January 2026

Edited by Meng-Jiao Zhou

Keywords:
Numerical simulation
Acoustic-elastic coupling equation
Ocean-bottom node
Four-component data
Scholte wave

ABSTRACT

The complex wavefields in ocean-bottom node (OBN) four-component (4C) seismic data, particularly interface waves like Scholte waves, pose significant challenges for processing and inversion. A key issue is how to achieve high-fidelity and accurate simulation of seismic wave propagation phenomena at the ocean bottom, thereby providing a theoretical foundation for fully leveraging ocean-bottom 4C data in imaging and inversion. To address this, we employ a three-dimensional acoustic-elastic coupling equation (AECE) for high-fidelity numerical simulation of OBN 4C data. This method inherently satisfies the fluid-solid interface conditions without manual enforcement, enabling physically consistent generation of all wave types, including Scholte waves. Numerical examples and field data from the East China Sea demonstrate that the AECE effectively replicates the waveform components and characteristics of field 4C data. This establishes the AECE as a robust foundation for OBN 4C data processing, elastic imaging, and full-waveform inversion.

1. Introduction

The main challenge in offshore oil and gas exploration remains that seismic data acquisition and seismic wave imaging cannot meet the accuracy requirements for reservoir identification, description, and evaluation (Xie et al., 2024). The “wide azimuth, wide frequency broadband, and high resolution” seismic data acquisition method is a widely recognized and effective technological approach for addressing the primary challenges in offshore oil and gas exploration (Wang et al., 2024a). Ocean-bottom node (OBN) acquisition is a widely recognized offshore seismic acquisition technology, distinguished by wide azimuth and frequency broadband, as well as high resolution (Pramik, 2013). However, compared to onshore oil and gas seismic exploration, the cost of densely deploying OBN is prohibitively high.

A significant amount of multi-component OBN seismic data has been acquired both domestically and internationally. However, compared to ocean bottom seismic acquisition technologies, the processing and interpretation techniques for ocean bottom four-component (4C) seismic data remain underdeveloped. Typically, the pressure component and vertical velocity component are treated as primary (P) waves, while the two horizontal velocity components are treated as converted shear (SV) waves. The P and SV waves are then processed and interpreted separately using the acoustic wave equation (Xie et al., 2017). This simplistic processing approach is far from sufficient for fully extracting information from 4C seismic records. The multi-wave imaging of OBN data essentially involves PP and PS wave imaging. However, no imaging results have been seen that effectively contribute to enhancing the accuracy of reservoir characterization. Regarding the issue of multi-wave imaging processing for OBN data, despite decades of exploration, the fundamental reason why multi-wave exploration has not been widely applied and has not generated significant exploration benefits is not essentially due to problems with seismic wave imaging theories and methods. Rather, it is because the wave phenomena observed in field multi-wave seismic wavefields do not match the theories of seismic wave propagation and simulation, leading to multi-wave imaging results that do not meet expectations (Li and Qu, 2022; Li et al., 2024). Therefore, it is

* Corresponding author.
** Corresponding author.
E-mail addresses: hhu_ypf@hhu.edu.cn (P.-F. Yu), czhang18@hhu.edu.cn (C. Zhang).

https://doi.org/10.1016/j.petsci.2025.12.038

essential to investigate the physical causes of the mismatch between the observed wave phenomena in the multi-wave seismic wavefields and the theories of seismic wave propagation and simulation.

Due to the presence of the seafloor interface, free surface, and seawater layer, as well as the influence of the varied seafloor environment, the waveform components of ocean bottom OBN multi-component seismic data are highly complex. Especially in shallow-water OBN multi-component data, guided waves and Scholte waves are strong (Kugler et al., 2007). Scholte waves are a type of interface wave that propagates along the boundary between a fluid and a solid medium. Their generation is a direct consequence of the coupling between the acoustic field in the fluid and the elastic field in the solid, particularly involving the solid's shear properties. These waves are excited when seismic energy interacts with the seafloor, and their existence is contingent on the shear wave velocity of the seabed being lower than the compressional wave velocity of the fluid (Scholte, 1947; Ewing et al., 1957). Meanwhile, it is difficult to distinguish between multiple waves related to the free surface and primary waves. This results in greater challenges for OBN data processing. Currently, there is relatively little research on the characteristics and influencing factors of OBN multi-component seismic data, and the understanding of these aspects is not clear enough. Wang et al. (2024b) constructed representative elastic parameter models based on varied water depths and typical seafloor sediment properties, and synthesized OBC/OBN multi-component seismic records using the spectral element method. They analyzed the characteristics of different wave components and revealed how water depth and seafloor medium properties influence the kinematic and dynamic characteristics of the wavefield. However, the numerical simulation of the seabed 4C seismic data was limited to two-dimensional (2D) medium.

Numerical simulation of the propagation of seismic waves in solid-fluid coupling media is crucial for analyzing ocean bottom 4C seismic data. The ocean bottom solid-fluid coupling problem refers to the issue of seismic wave propagation through the interface between solid and liquid media. Accurately simulating the propagation of seismic waves through solid-liquid interfaces enables the correct study of physical phenomena associated with the solid-liquid interface, such as the propagation of Scholte waves (Carcione and Helle, 2004; Xu et al., 2022; Yu et al., 2024) and low-frequency seismo-acoustic waves (Lecoulant et al., 2022), and the scattering problem of seafloor topography (Greaves and Stephen, 2000; Zhen et al., 2023). The main challenge in the numerical simulation of ocean bottom 4C seismic data is the lack of a wave equation that describes the propagation of the 4C data. Ocean bottom 4C seismic data includes both acoustic pressure component in the seawater and three velocity components in the elastic seafloor. Neither the acoustic wave equation nor the elastic wave equation can simultaneously describe the propagation of the pressure component and the three velocity components. If the acoustic wave equation is used in seawater, while the elastic wave equation is applied to the elastic medium at the seabed, continuity conditions for displacement and stress must be satisfied at this interface (Zhang, 2004; Carcione et al., 2018; Qu et al., 2023). When employing the finite difference (FD) method to solve the wave equations, it becomes challenging to handle cases with a sharply undulating seafloor (Zou et al., 2020; Sun et al., 2021). To address this challenge, Xia et al. (2024) proposed a coupled LBM-LSM scheme to model seismic wavefields across a more realistic rugged seabed. However, this method cannot accurately describe the propagation of the four-component data at the fluid-solid interface simultaneously. If the elastic wave equation is used in both the fluid and solid media, the shear (S) wave velocity is set to 0 in the fluid (acoustic) medium (Virieux, 1986). This method ensures the continuity of the velocity at the interface, but the Poisson's ratio must be less than 0.5 to ensure computational stability (Qu et al., 2015). Yu et al. (2016) first proposed simulating the propagation of ocean bottom 4C data by constructing a set of acoustic-elastic coupling equations (AECE), which avoids to explicitly impose displacement and continuity conditions at the interface. Li et al. (2023) developed a mesh-less AECE forward modeling method. Bader et al. (2023) used energy-stable summation-by-parts operators for modeling in acoustic-elastic coupled media. In recent years, many scholars have extended the application of AECE from isotropic media to anisotropic media (Yu and Geng, 2019; Zhang et al., 2023; Chen and Wang, 2024). This paper aims to clarify the compositional characteristics and propagation mechanisms of the 4C wavefields in OBN surveys through three-dimensional (3D) numerical simulation, which may be helpful to the development and application of OBN multi-component data processing techniques.

2. Modeling and analysis of OBN multicomponent seismic data

2.1. A 3D two-layer model

A two-layer horizontal seawater-seabed model is built where the first layer is seawater and the second layer is an elastic medium. The model parameters are shown in Table 1. The AECE and the acoustic equations are used for ocean bottom multi-component simulation, respectively. A Ricker wavelet with a dominant frequency of 20 Hz is used as the source (S), placed below the sea surface at coordinates (0.05 km, 0.375 km, 0.01 km). The receiver is located at coordinates (0.7 km, 0.375 km, 0.1 km). To avoid the influence of multiple reflections on the wavefield

Table 1
Elastic geological parameters of the two-layer seawater-seabed model.

Layer number	Layer thickness, m	V_p, m/s	V_s, m/s	ρ, kg/m^3
1	100	1500	0	1050
2	650	2000	1000	1500

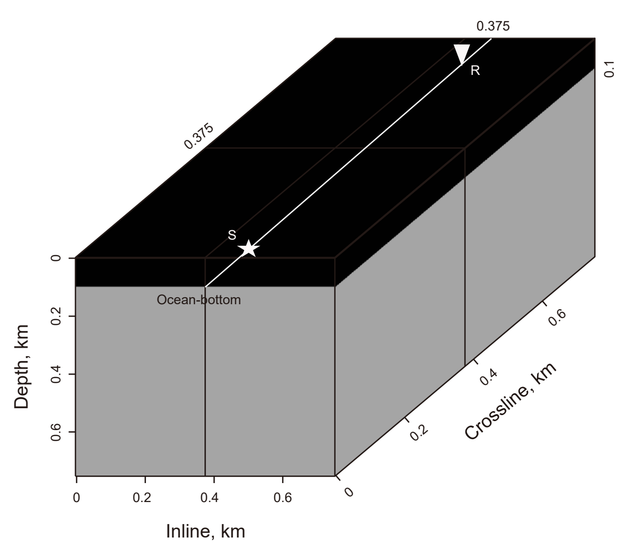

Fig. 1. Schematic diagram of numerical simulation for a two-layer seawater-seabed model (☆ indicates the location of the seabed source; ▽ indicates the location of the seabed receiver).

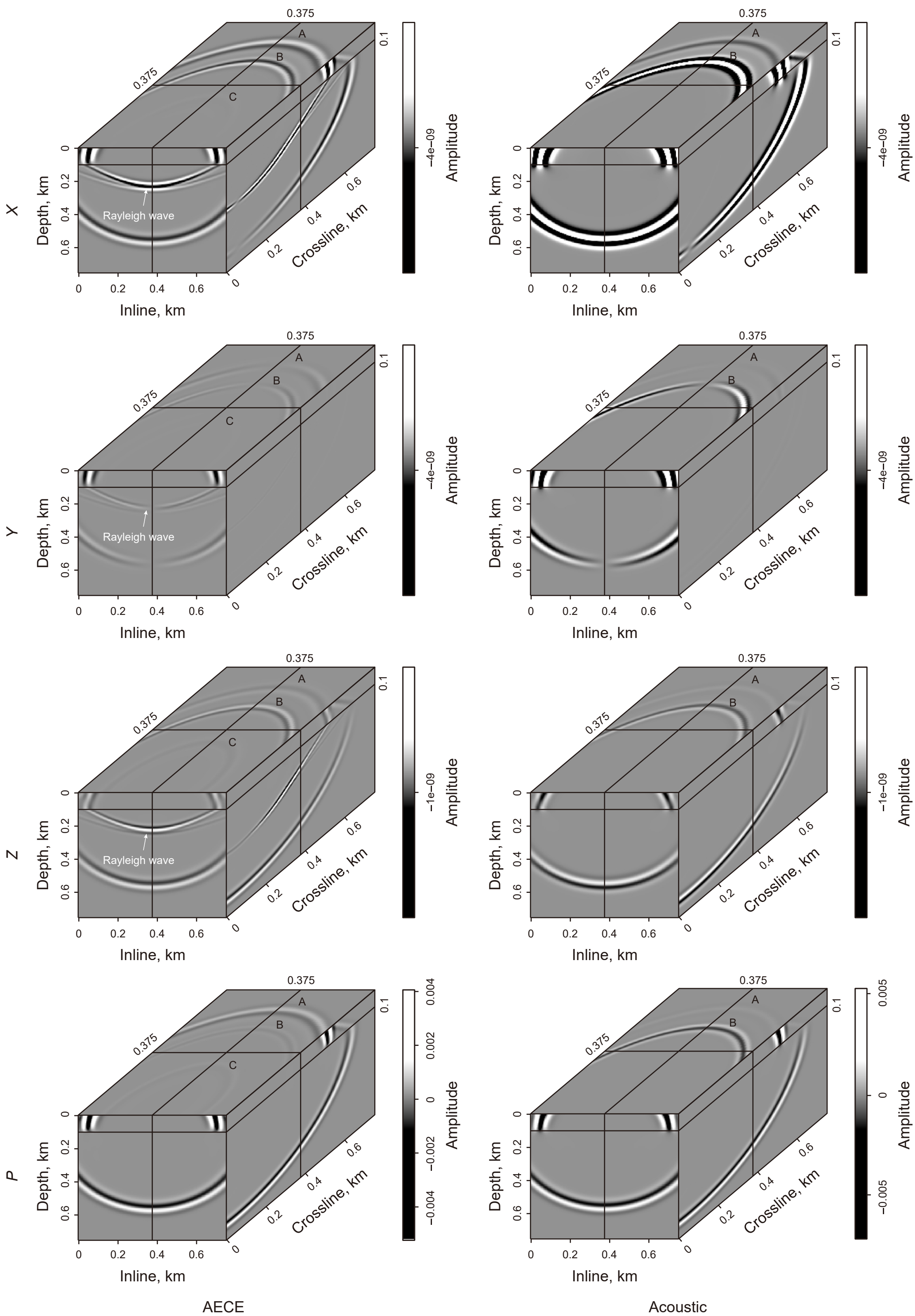

Fig. 2. Snapshots of simulated 4C at $t = 0.35$ s based on the AECE and the acoustic equation, respectively.

analysis, a CPML boundary is set at the sea surface (Tang et al., 2022). The schematic diagram of the observation system is shown in Fig. 1.

2.2. Characteristic analysis

Fig. 2 shows the simulated 4C snapshots at $t = 0.35$ s using the AECE and the acoustic equation, respectively. In Fig. 2, event "A" represents the first arrival wave, event "B" represents the direct wave, and event "C" represents the Scholte wave. In the 4C snapshots simulated using the acoustic equation, neither S-waves nor Scholte waves were observed. To provide more direct evidence of the Scholte wave as an interface wave, Fig. 3 displays a series of wave-field snapshots at different time steps. Event "C" is clearly observed propagating horizontally along the fluid-solid interface, which is the defining kinematic characteristic of a guided interface wave, thus confirming its identity. Comparisons of seismograms extracted at location R from simulated snapshots are shown in Fig. 4. The waveforms and phase characteristics of the multi-component records simulated with two equations exhibit significant differences.

The hydrophone records the pressure component in the water just above the fluid-solid interface, while the three-component geophone records the displacement (velocity) components in the solid just below the fluid-solid interface. Based on the AECE, numerical modeling can be used to investigate the continuity characteristics of displacements (velocity) and stresses at the seabed fluid-solid interface (Fig. 5). The comparison results show that the vertical velocity component and the vertical normal stress have similar waveforms at the fluid-solid interface. Both components are continuous at the fluid-solid interface (as indicated by the rectangular boxes). The X component and the pressure component exhibit significant waveform differences at the fluid-solid interface, and both components are discontinuous at the fluid-solid interface. Since the geophone R is located along the shot-receiver line, the energy of the Y component is almost zero (Fig. 5(a)). As the seabed is horizontal, the negative vertical normal stress is equal to the pressure in the seawater just above the seabed. Some obvious differences in the waveform characteristics at the fluid-solid interface are observed between the pressure component and the P component obtained through Helmholtz decomposition (Fig. 5(b)). The wavefield characteristics of the simulated results at the fluid-solid interface are consistent with the theoretical Eqs. (B-4) and (B-5).

It is generally accepted that hydrophones and geophones detect signals just above (in seawater) and below (within submarine

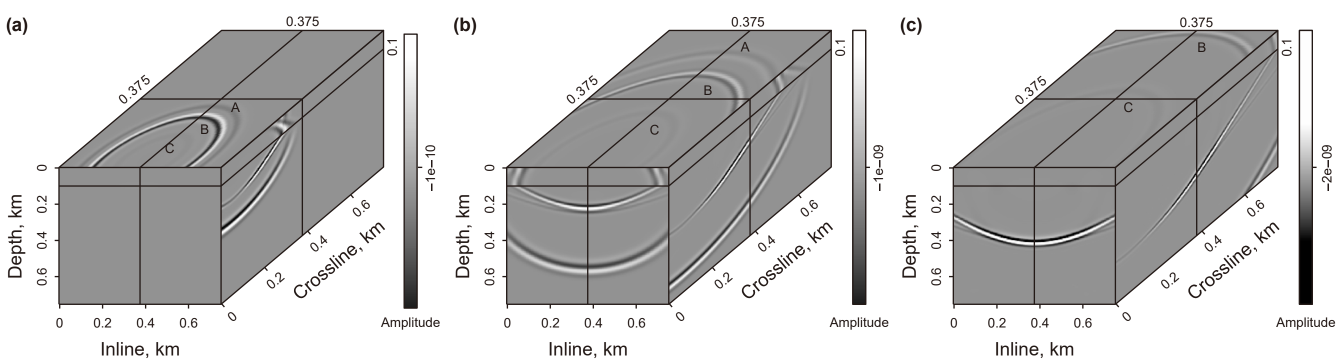

Fig. 3. Snapshots of simulated Z component at (**a**) $t = 0.20$ s, (**b**) $t = 0.35$ s, and (**c**) $t = 0.50$ s based on the AECE, respectively.

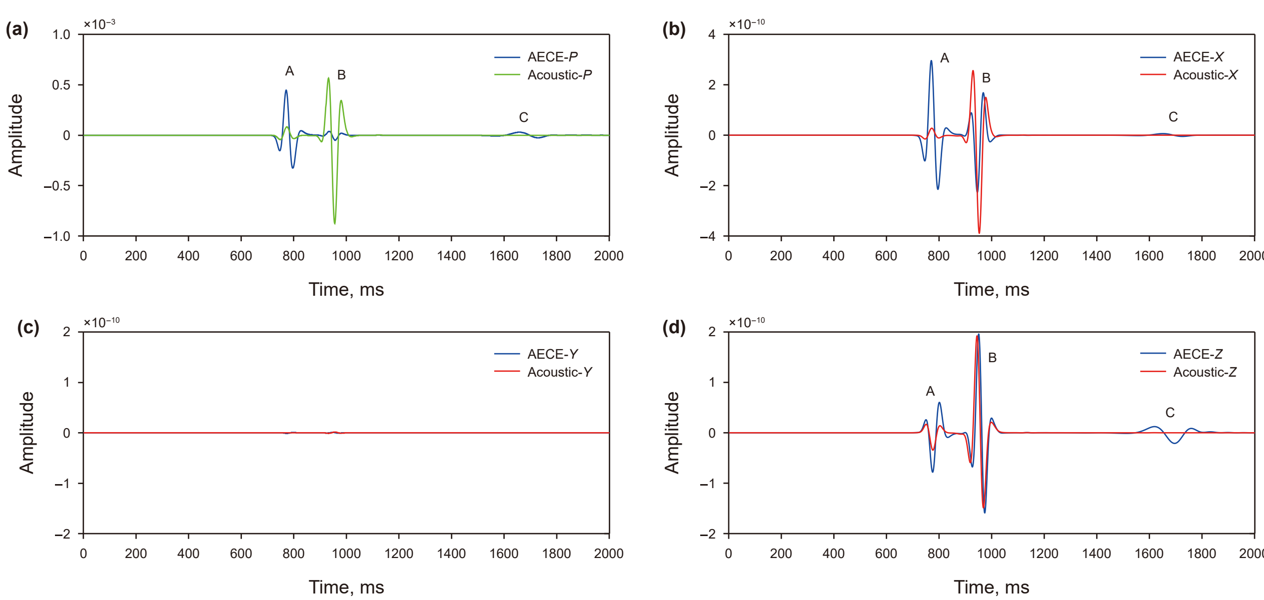

Fig. 4. Seismograms modeled using the AECE and acoustic equation at the receiver R indicated in Fig. 1: (**a**) the pressure component, (**b**) the horizontal X, (**c**) the horizontal Y, and (**d**) the vertical Z components. The labels correspond to the same arrivals indicated in Fig. 2.

sedimentary strata) the seabed interface, respectively. As shown in Fig. C-1 of Appendix C for the two-dimensional scenario, when a P-wave is generated by a seismic source in seawater, the incident down-going P-wave undergoes reflection, transmission, and mode conversion at the seabed interface. Consequently, the hydrophone above the interface records both the incident wave and the reflected P-wave, while the geophone below the interface captures the transmitted and converted waves. The specific characteristics of different wave types in multicomponent recordings are closely related to the properties of the seabed. Variations in the elastic parameters of submarine media lead to changes in the reflection, transmission, and conversion coefficients of elastic waves, thereby influencing the energy distribution relationships among different wave types at the interface. The reflection/transmission coefficients for P- or S-waves can be seen in Appendix C.

Based on the model parameters (Table 1), the curves of reflection and transmission coefficients versus incident angle were calculated. It was found that when a down-going P-wave is incident (Fig. 6), the P-wave reflection coefficient is approximately 0.3, the transmission coefficient is approximately 0.7, and the P-S conversion coefficient increases with increasing incident angle. Similarly, the energy of Scholte waves gradually strengthens as the incident angle grows.

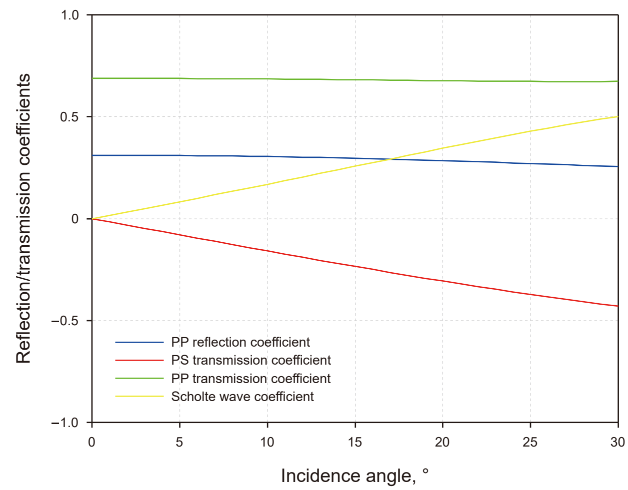

Fig. 6. Seabed reflection/transmission coefficients vs. incident angle.

2.3. The complex model experiment

We used a 3D modified Overthrust model for ocean bottom 4C data numerical experiment. Fig. 7 depicts P- and S-wave velocities and density models composed of a water layer and a series of sediments layers. A shot of compressional source was fired at the sea surface (white star in Fig. 7), and the wavefields were recorded by two horizontal arrays of receivers placed at the seabed. The data were simulated with free-surface-related multiples.

Fig. 8 displays the common-shot gathers (CSGs) of the two receiver lines, revealing the following characteristics: (1) Distinct

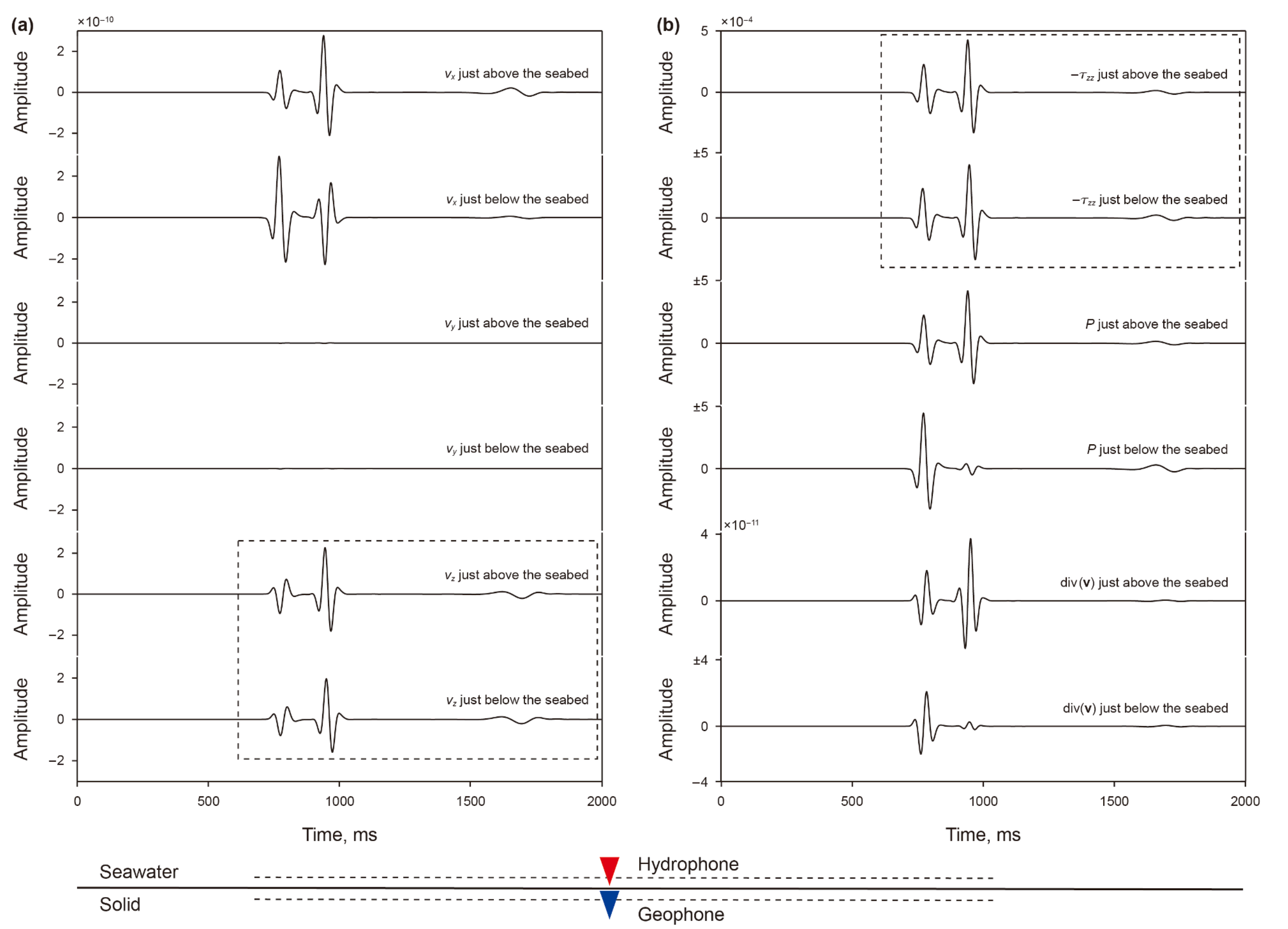

Fig. 5. Comparison of multi-component data extraction just above and below the seabed: (**a**) three velocity components, (**b**) the vertical normal stress and P components.

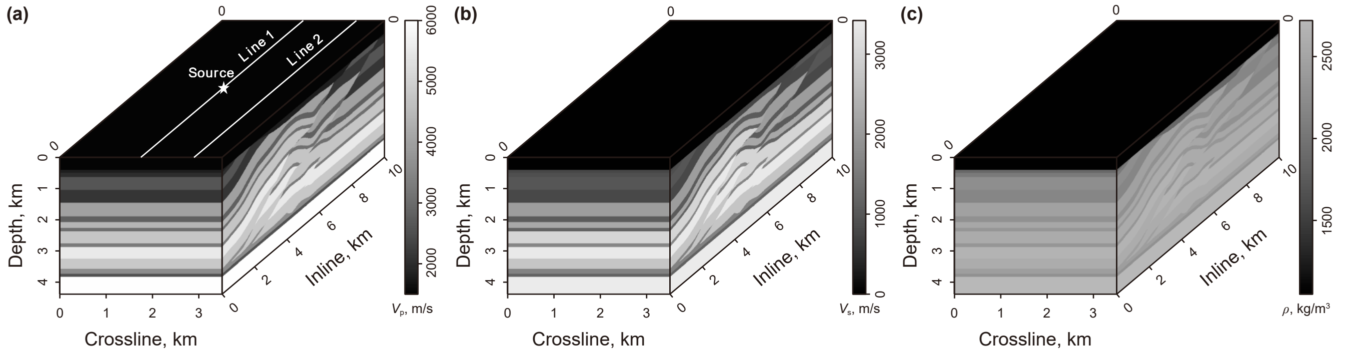

Fig. 7. Schematic diagram of numerical simulation for the 3D modified Overthrust model (☆ indicates the location of the source; two solid white lines represent the OBN survey lines at the seabed).

Scholte waves are observed in the simulated CSGs; (2) The multiples generated by the free surface exhibit strong energy, with first-order and higher-order multiples clearly visible in the CSGs. In the pressure component, the primary energy consists of P-waves, with almost no observable S-waves. Although some P-waves are visible on the *X* component, S-waves dominate overall. Since Line 1 lies in the same plane as the shot-receiver line, the energy of seismic signals recorded on the *Y* component of Line 1 is very weak, with only some SH-waves being distinctly observed. In contrast, Line 2 is not coplanar with the shot-receiver line, allowing clear observations of both P-waves and S-waves (SV- and SH-waves) in the *Y* component (Fig. 9).

3. Field data example

3.1. 3D OBN data acquisition in the East China sea

In 2017, a joint project involving CNOOC, Tongji University, and Sinopec conducted a 3D OBN 4C seismic data acquisition in the QY shallow-water work area of the East China Sea, with a seawater depth of approximately 82 m. The OBN (GOBS) used was developed by the Institute of Geology and Geophysics, Chinese Academy of Sciences. A total of 100 OBNs were deployed on the seabed at 100 m intervals. The data recording length was 6 s, with a sampling interval of 0.5 ms. The frequency band of the air gun source signal ranges from 5 Hz to 88 Hz, with a source excitation interval of 37.5 m. The OBN acquisition system is shown in Fig. 10.

3.2. Numerical simulation of the East China Sea model

Wang et al. (2020) used the Scholte waves from the ocean bottom 4C data of the East China Sea to perform S-wave velocity inversion for the shallow sediments, and obtained the P-wave and S-wave velocities, as well as the stratigraphy information of the sediments in the survey area (Table 2). Based on the inverted stratigraphic elastic parameters (Wang et al., 2020), a 3D geological model was constructed. 3D numerical simulation of ocean bottom 4C seismic data was conducted using the AECE. To facilitate comparative analysis with the actual common-receiver gathers (CRGs) data from node S002, a Ricker wavelet with a dominant frequency of 20 Hz was placed directly above node S002 at the sea surface as the seismic source. Three receiver lines were deployed on the seafloor to acquire simulated ocean-bottom 4C data. These three simulated receiver lines were positioned directly beneath the three actual shot lines (Line 1, Line 2, and Line 3). Using this acquisition geometry, the simulated CSGs of the ocean-bottom 4C data were compared and analyzed against the actual CRGs from node S002. The spatial grid spacing was 2 m, with a time sampling interval of 0.2 ms. Three CSGs records with an inter-line spacing of 200 m were simulated (the observation system is shown in Fig. 10(b)).

3.3. Comparison of the simulated and field 4C data

Fig. 11 displays the simulated and field *Z* components. Due to the relatively shallow water depth, free-surface-related multiples are highly developed. In the *Z* component, P-wave energy dominates. Since we use a Ricker wavelet with a dominant frequency of 20 Hz as the source for numerical simulation, Scholte waves are not observed in the simulated records (Fig. 11(a)–(c)); however, in the field *Z* component, weaker-energy Scholte waves can be observed (Fig. 11(d)–(f)). In the *Y* component, SH-waves are predominantly observed (Fig. 12). Neither in the simulated *Y* component nor in the field *Y* component are there any significant Scholte waves observed. In the *X* component, S waves are predominantly observed, with a noticeable polarity reversal occurring at zero offset (Fig. 13). Similarly, no significant Scholte waves are observed in the *X* component.

Fig. 14 shows the simulated and field pressure components. The pressure component is predominantly composed of P waves. In the field pressure component, multiples are well-developed, making it difficult to distinguish from the primary reflected waves. As the hydrophone cannot record low-frequency components below 5 Hz, Scholte waves are not observed in the pressure records. The waveform components and characteristics of the ocean bottom 4C data from numerical simulation and field acquisition are generally similar. However, there are some differences, primarily due to the discrepancy between the wavelet in numerical simulations and the seismic wavelet in field data.

Frequency spectrum analysis was performed on the simulated and field pressure components and *Z* components of Line 2 (Fig. 15). The results show that only the spectrum of the field *Z* component exhibits an energy peak in the low-frequency range (<10 Hz), while Scholte waves are low-frequency (<5 Hz). Therefore, weaker Scholte waves can only be observed in the field *Z* component. For the field *Z* component and pressure component, multiple peaks are observed, indicating the presence of multiple notch points, which differs from the results of the numerical simulation.

Due to the presence of the free surface between seawater and air, ocean bottom multi-component seismic data contain various wave types associated with surface-related effects, including source-side ghosts, source-side multiples, and receiver-side multiples. Among these, the delayed components at certain frequencies happen to be integer multiples of the period of the corresponding harmonic components in the primary reflection wave. As a result, they interfere destructively with the primary wave, leading to notch phenomena in the data frequency band. The

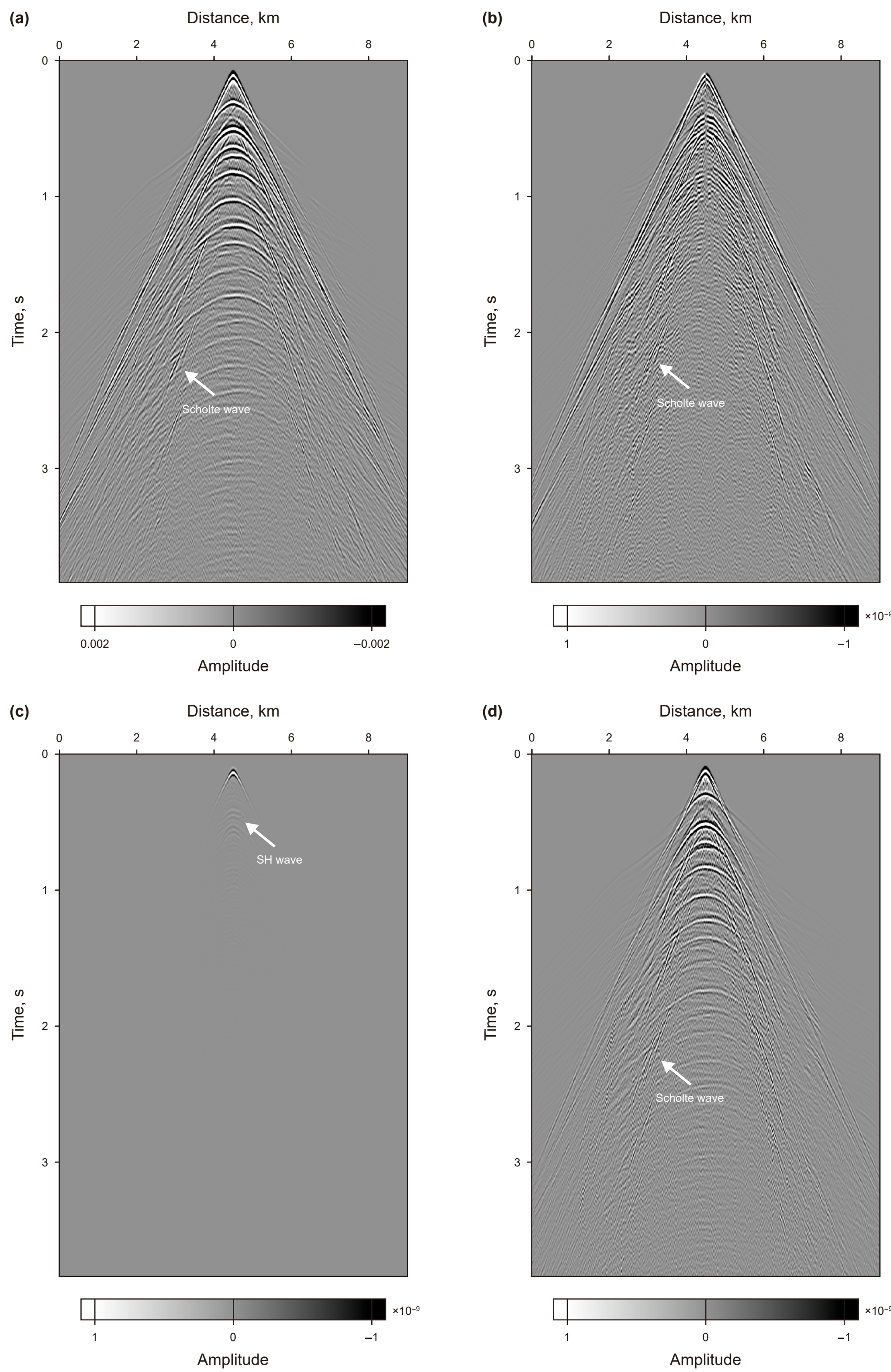

Fig. 8. Simulated 4C records of Line 1 based on the AECE: (**a**) *P* component; (**b**) *X* component; (**c**) *Y* component; (**d**) *Z* component.

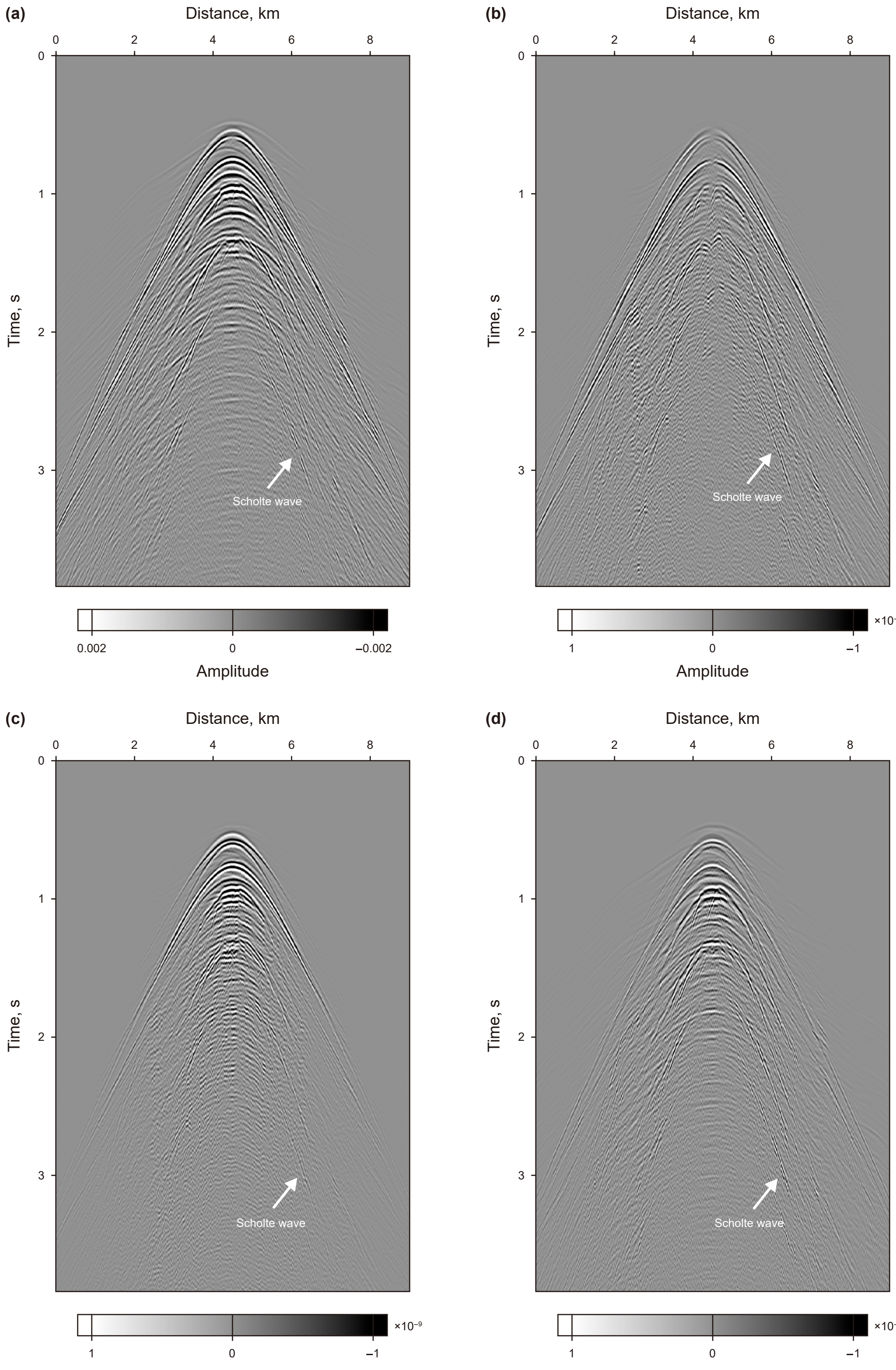

Fig. 9. Simulated 4C records of Line 2 based on the AECE: (**a**) *P* component; (**b**) *X* component; (**c**) *Y* component; (**d**) *Z* component.

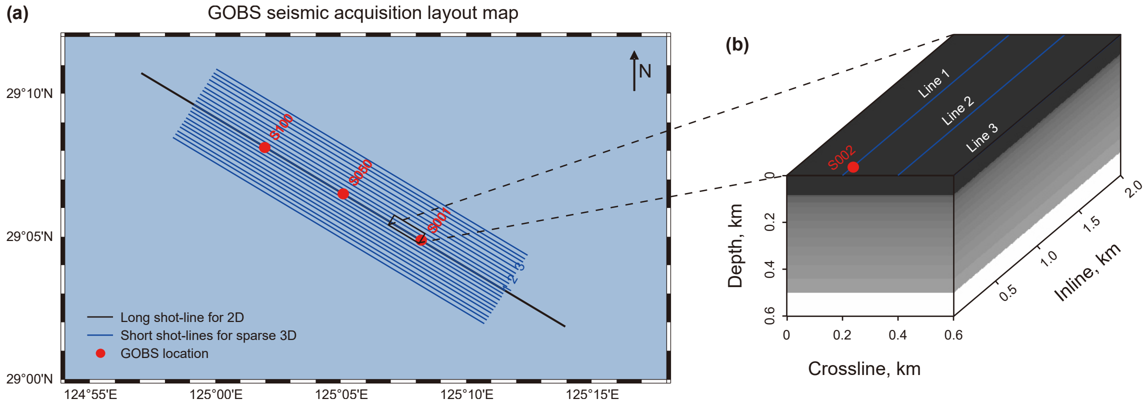

Fig. 10. Schematic diagram of field GOBS acquisition and numerical simulation of the East China Sea model.

Table 2
Elastic parameters of the shallow sediments in the East China Sea.

Layer number	Layer thickness, m	V_p, m/s	V_s, m/s	ρ, kg/m^3
1	82	1500	0.00	1030
2	10	1580	201.8	1744
3	20	1600	238.0	1801
4	30	1620	307.8	1891
5	30	1630	343.3	1929
6	30	1640	351.0	1936
7	30	1650	404.4	1985
8	40	1660	465.4	2034
9	40	1670	489.4	2052
10	40	1680	554.0	2095
11	40	1690	556.1	2096
12	59	1700	597.7	2121
13	59	1720	632.9	2141
14	∞	1800	667.0	2159

theoretical formula for calculating notch points at near-offsets can be approximately expressed as (Wang et al., 2024b):

$$f = \frac{nc}{2z}. \tag{1}$$

where $n = 0, 1, 2, 3 \ldots$ represents the notch index, c denotes the acoustic velocity in water, and z represents the source depth or the receiver depth. From the amplitude spectrum of the P-component (Fig. 15), it can be observed that the frequencies corresponding to the amplitude minima are approximately 12 and 24 Hz, which generally align with the theoretical notch positions. Meanwhile, we observed significant discrepancies in the notch frequencies between the simulated and actual data across different components (Fig. 15). These differences may be attributed to various factors, such as environmental noise, sensor imperfections, multiples, and ghost waves.

Low-pass filtering was applied to the three velocity components from both numerical simulation and field acquisition. Fig. 16 shows the simulated and field X components after low-pass filtering. Both datasets exhibit nearly identical waveform components and characteristics, and distinct Scholte waves can be observed in both components. After the low-pass filtering, distinct Scholte waves can be observed in both the numerically simulated and field Y component of the Line 2 and Line 3 (Fig. 17). However, Scholte waves are not observable in the Line 1. This is due to the fact that node S002 lies in the plane of Line 1. For the Z component after low-pass filtering, Scholte waves can be clearly observed on all three shot lines (Fig. 18). Compared to the filtered X and Y components, the Scholte waves exhibit stronger energy and more pronounced dispersion characteristics.

The ability to generate a complete and realistic wavefield is confirmed by the strong correspondence between the AECE-simulated results and the field data from the East China Sea (Figs. 11–18). The simulation successfully captures the essential waveform characteristics of the field data, including the low-frequency Scholte waves. This direct alignment with real-world measurements serves as the ultimate validation of the method's high fidelity.

4. Discussions

The fundamental advantage of the AECE method lies in its treatment of the fluid and solid domains as a unified, coupled system, solved simultaneously within a single framework. This approach natively and automatically satisfies all boundary conditions at the fluid-solid interface. In contrast, traditional methods solve two separate systems and then attempt to “stitch” or “convert” wavefields at the boundary, inevitably introducing errors and physical inconsistencies.

The P component simulated using the acoustic equation in water and elastic equation in solid method (A&E method for short) is similar to the pressure component above the seabed simulated based on the acoustic wave equation, with an absence of the Scholte waves. (Fig. 19). P component derived with Helmholtz decomposition is a mathematical equivalent, not the true physical pressure. Its amplitude, phase, and physical dimensions inherently differ from the true pressure field. As shown in Fig. 19(a), P component derived with Helmholtz decomposition differs significantly from the measured pressure record in both amplitude and phase. This makes it unsuitable for amplitude-critical applications like waveform inversion and true-amplitude imaging. In the water layer, AECE directly solves for the fluid pressure. This pressure is precisely the data recorded by the OBN hydrophone. Therefore, the P component simulated by AECE requires no conversion or decomposition and can inherently be directly and accurately compared and matched with field-acquired P component data (as shown in Fig. 14). This inherent amplitude fidelity makes AECE-simulated data ideally suited as input for reverse time migration and full waveform inversion, enabling reliable inversion of subsurface properties.

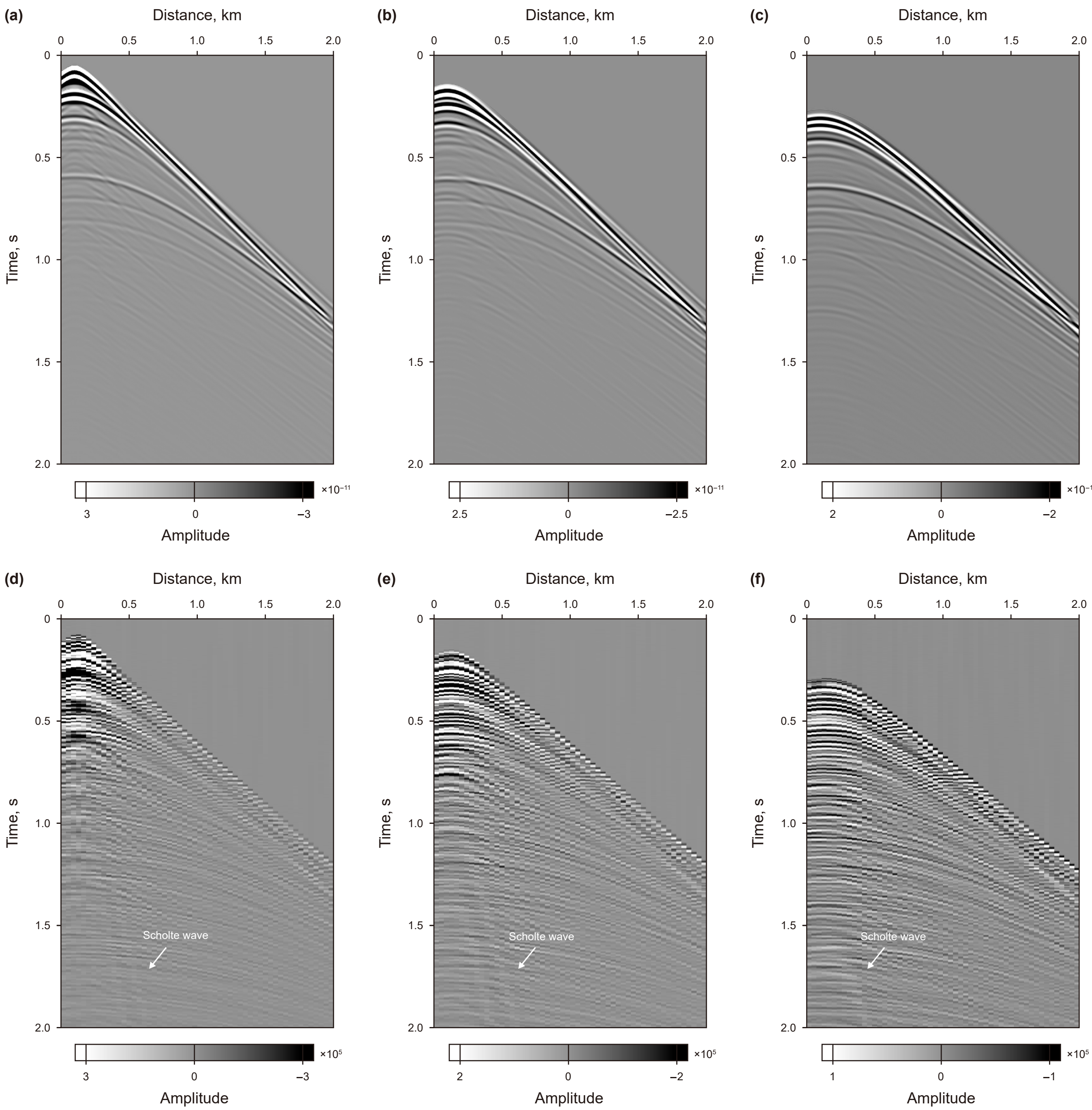

Fig. 11. Comparison of the simulated (**a**, **b**, **c**) and field (**d**, **e**, **f**) *Z* components: (**a**, **d**) Line 1, (**b**, **e**) Line 2, and (**c**, **f**) Line 3.

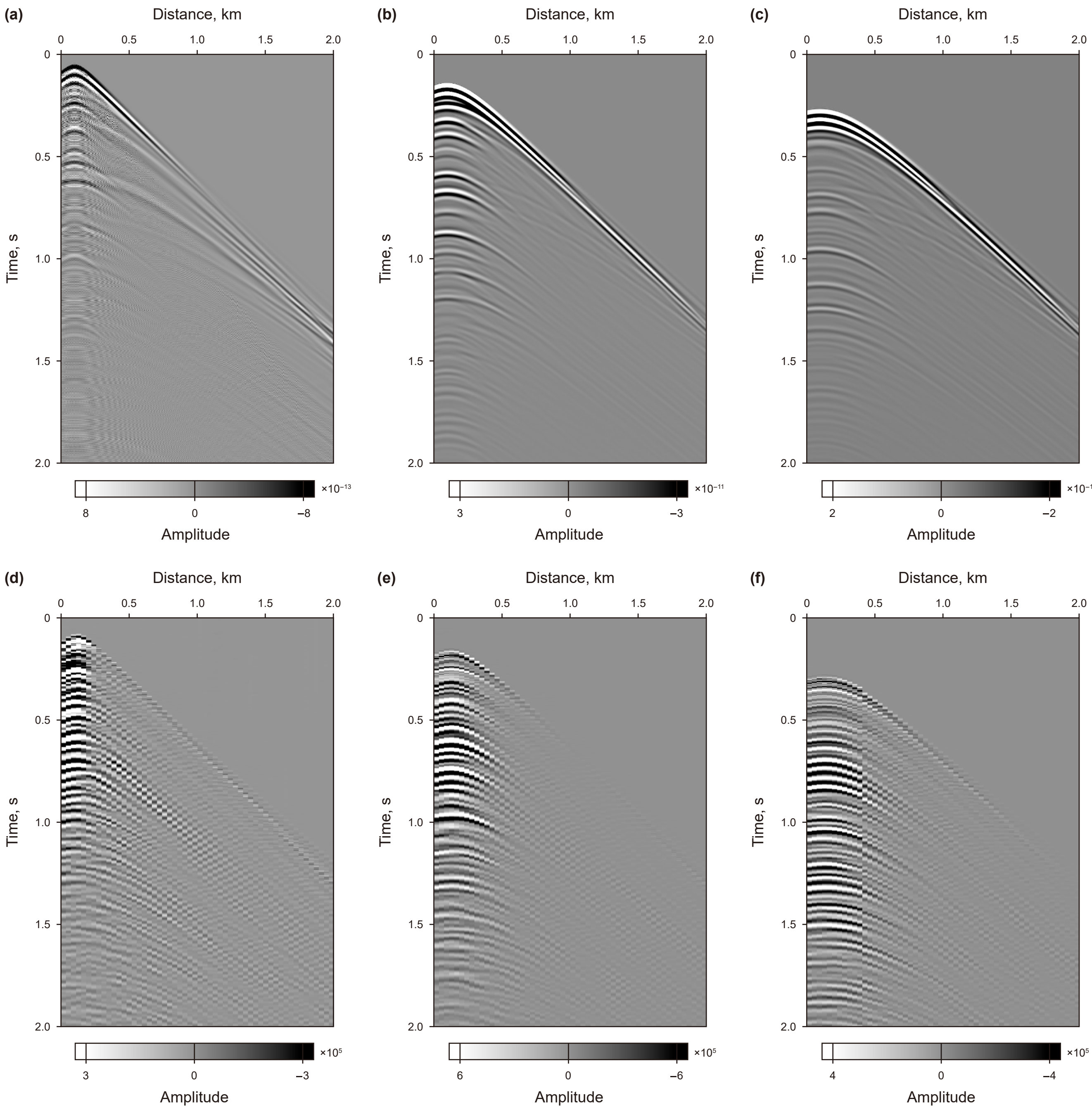

Fig. 12. Comparison of the simulated (**a**, **b**, **c**) and field (**d**, **e**, **f**) *Y* components: (**a**, **d**) Line 1, (**b**, **e**) Line 2, and (**c**, **f**) Line 3.

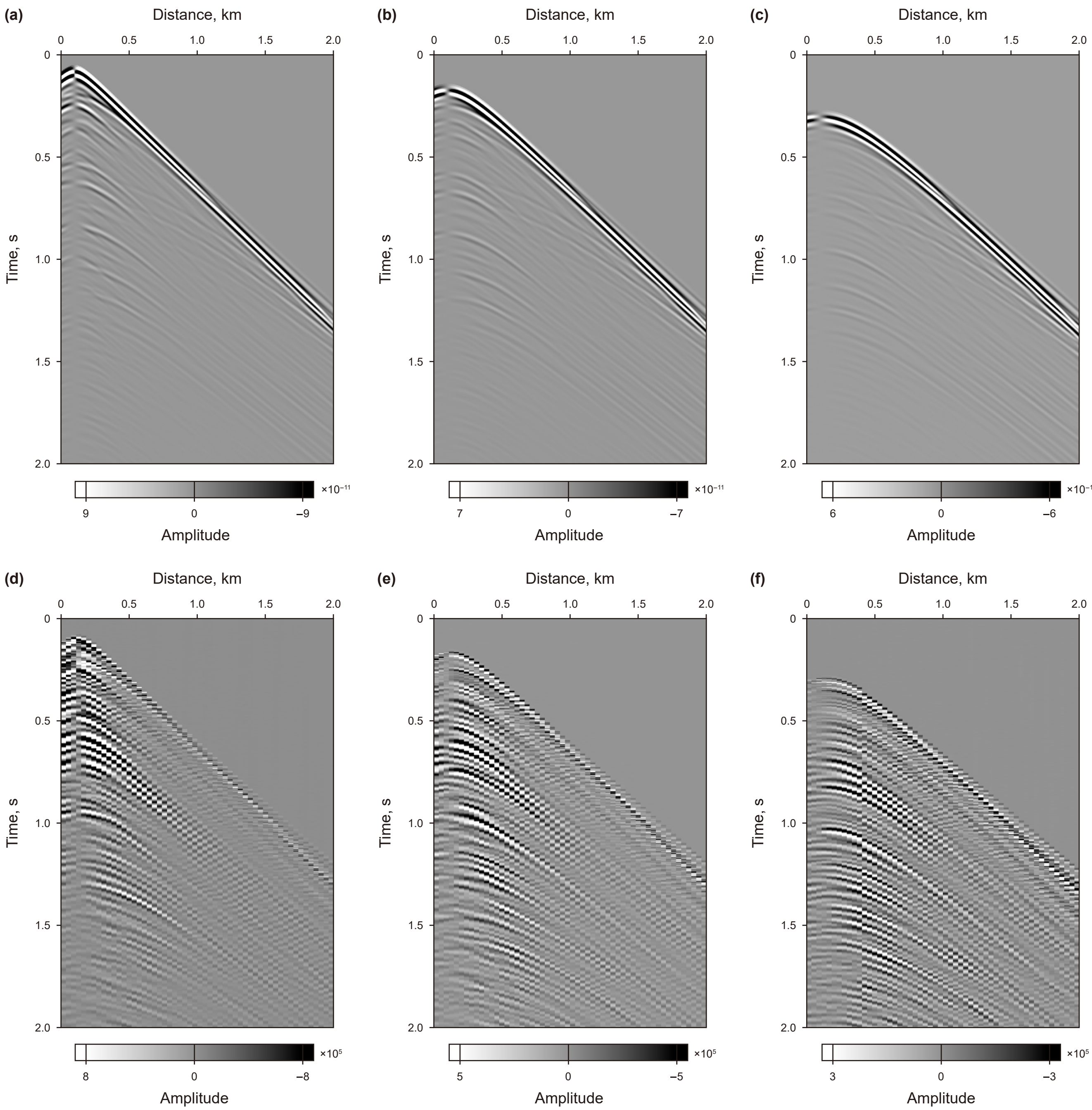

Fig. 13. Comparison of the simulated (**a**, **b**, **c**) and field (**d**, **e**, **f**) *X* components: (**a**, **d**) Line 1, (**b**, **e**) Line 2, and (**c**, **f**) Line 3.

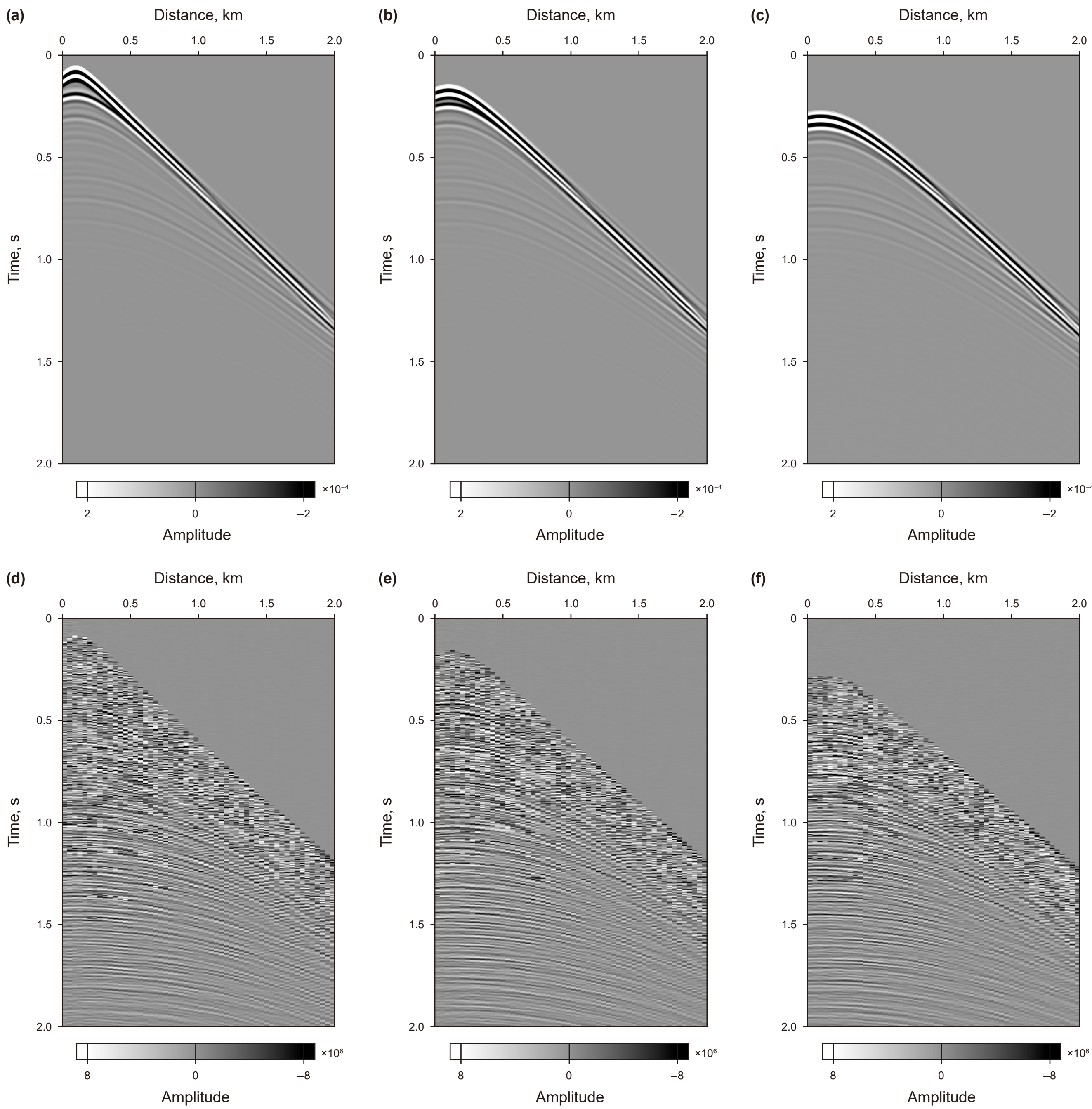

Fig. 14. Comparison of the simulated (**a**, **b**, **c**) and field (**d**, **e**, **f**) *P* components: (**a**, **d**) Line 1, (**b**, **e**) Line 2, and (**c**, **f**) Line 3.

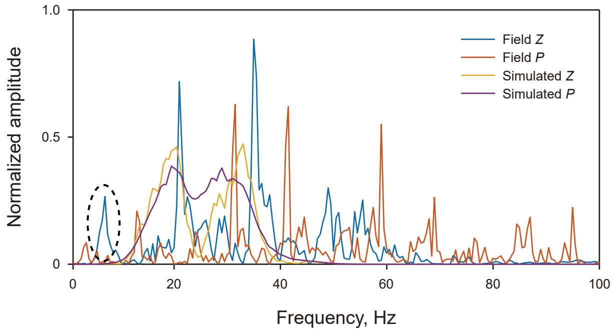

Fig. 15. Amplitude spectra of seabed *P* components and *Z* components for Line 2 from numerical simulation and field acquisition.

Using purely acoustic equations for seawater completely fails to generate S-waves and Scholte waves (as shown in Fig. 4). Even using elastic equations and setting the fluid as an "acoustic-elastic" medium with $V_s = 0$ m/s, the process of manually handling boundaries is complex and struggles to accurately simulate the excitation and propagation of Scholte waves. Helmholtz decomposition disrupts the coupled wavefield relationship at the interface, leading to inaccurate Scholte wave energy and dispersion characteristics. AECE naturally and precisely simulates all wave conversions. Scholte waves are interface waves strictly dependent on the coupled vibration of the fluid and solid. The mathematical formulation of AECE describes this coupling itself, thus enabling the spontaneous generation of physically realistic Scholte waves (e.g., event C in Fig. 4).

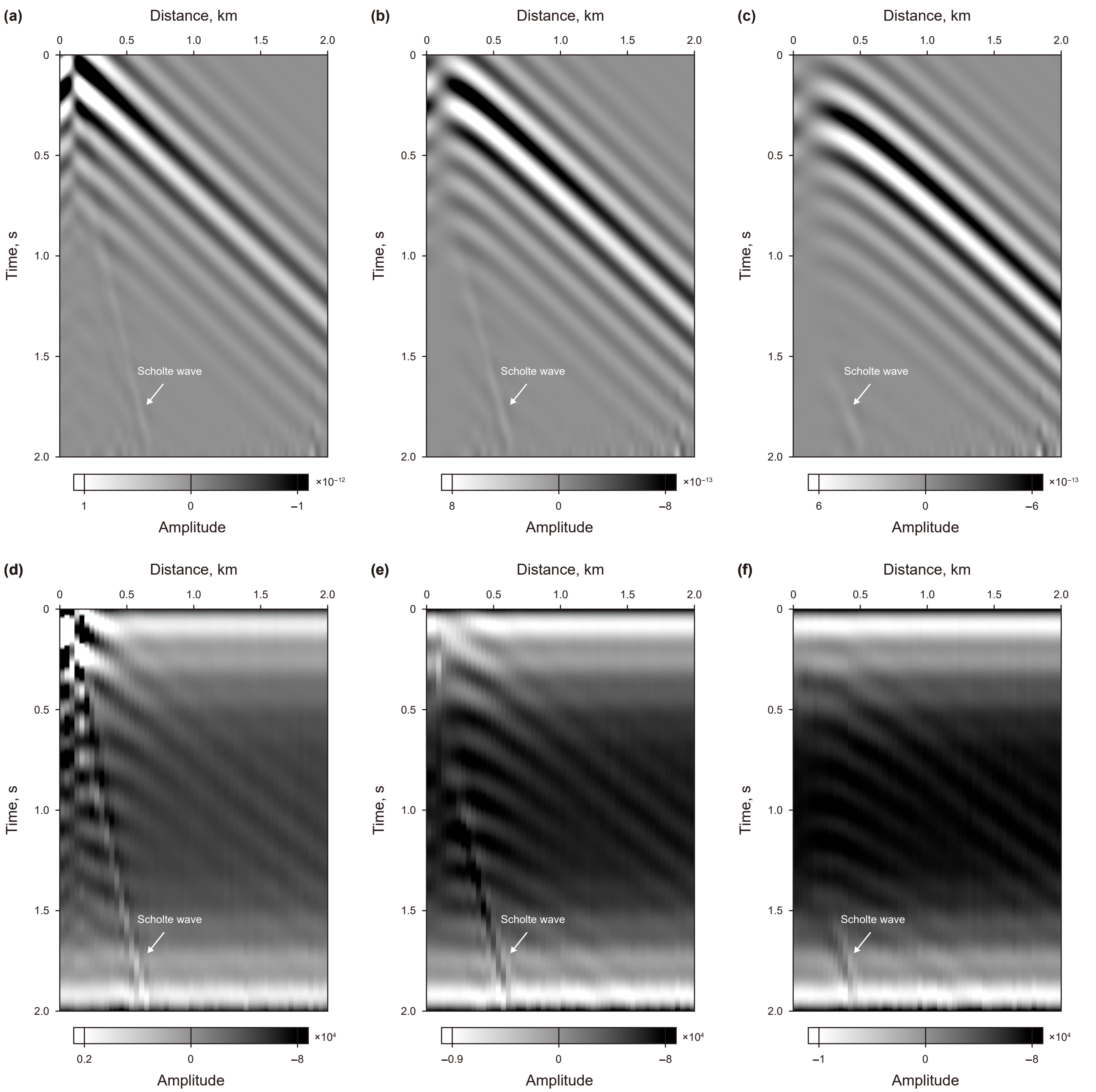

Fig. 16. Comparison of the simulated (**a**, **b**, **c**) and field (**d**, **e**, **f**) *X* components after low-pass filtering: (**a**, **d**) Line 1, (**b**, **e**) Line 2, and (**c**, **f**) Line 3.

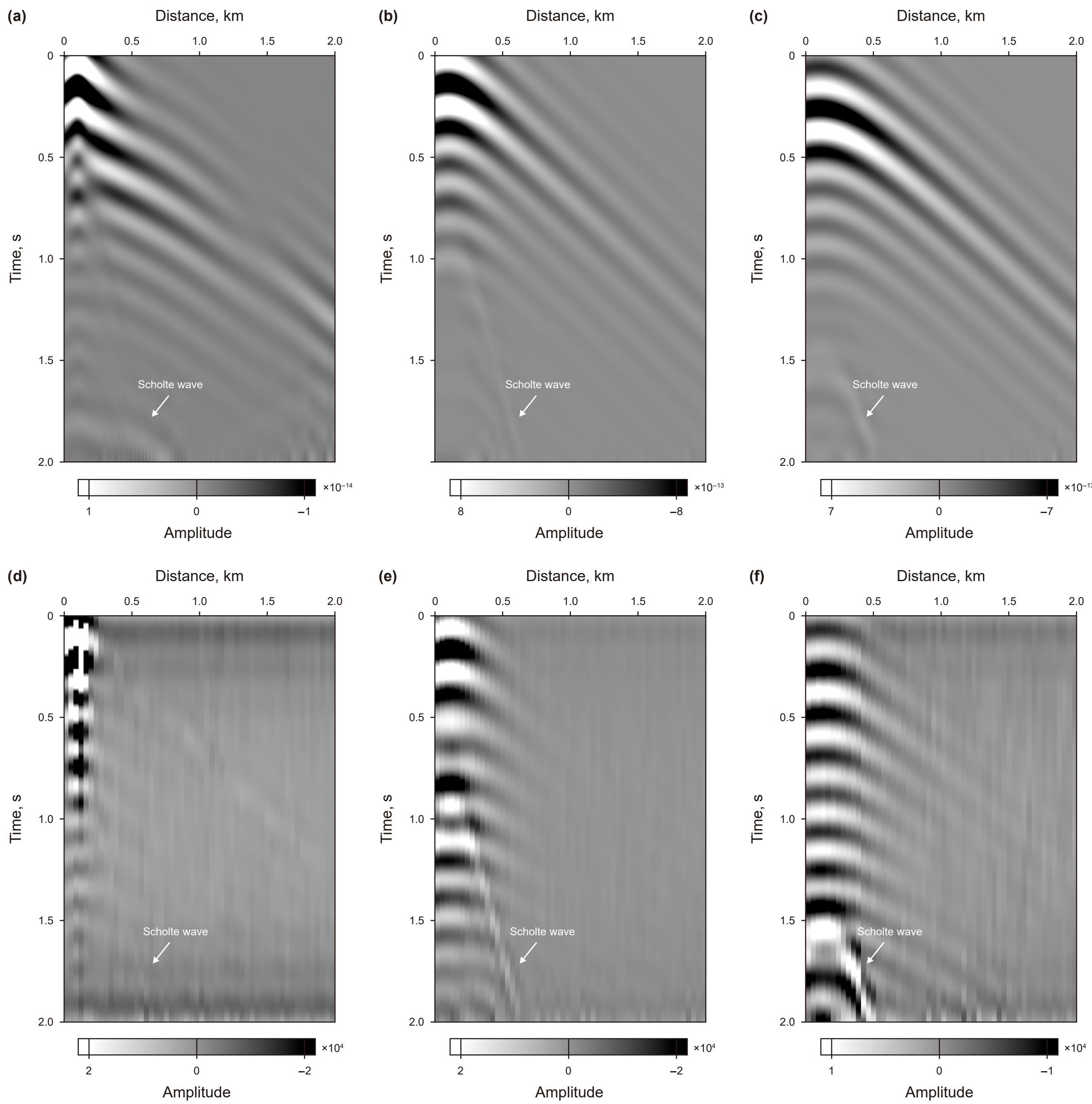

Fig. 17. Comparison of the simulated (**a**, **b**, **c**) and field (**d**, **e**, **f**) *Y* components after low-pass filtering: (**a**, **d**) Line 1, (**b**, **e**) Line 2, and (**c**, **f**) Line 3.

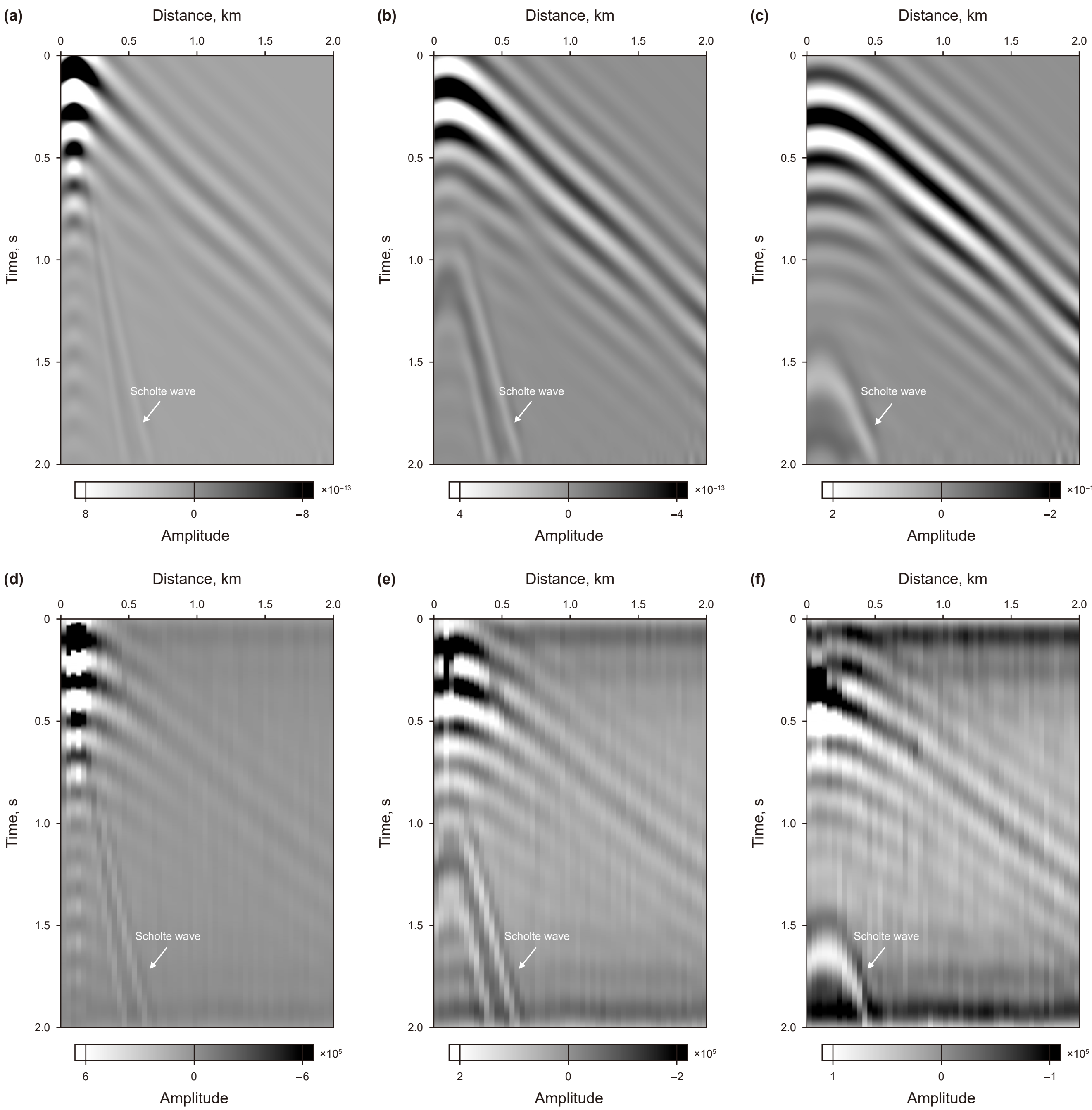

Fig. 18. Comparison of the simulated (**a**, **b**, **c**) and field (**d**, **e**, **f**) *Z* components after low-pass filtering: (**a**, **d**) Line 1, (**b**, **e**) Line 2, and (**c**, **f**) Line 3.

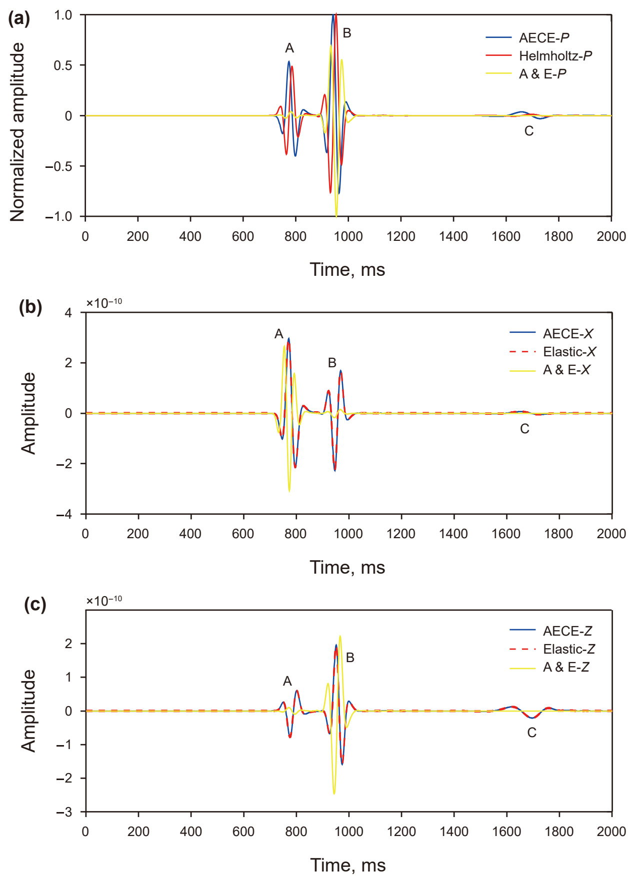

Fig. 19. Comparisons of ocean-bottom seismograms modeled using the AECE with other traditional methods at the receiver R indicated in Fig. 1: (**a**) The *P* component just above the fluid-solid interface, (**b**) the horizontal *X* and (**c**) vertical *Z* components just below the fluid-solid interface. A&E stands for using the acoustic wave equation for seawater and the elastic wave equation for the seabed in numerical simulations.

Only one set of code, one system is needed to simulate the entire water-seabed model, eliminating the need to switch or transfer data between acoustic and elastic domains. Because boundary conditions are automatically satisfied, the AECE method is more robust for handling rugged seafloor topography. Traditional methods struggle with applying complex boundary conditions at irregular interfaces.

5. Conclusions

This study demonstrates the effectiveness of the AECE for high-fidelity numerical simulation of ocean-bottom 4C seismic data. The AECE inherently satisfies the fluid-solid boundary conditions without manual intervention, enabling physically consistent simulation of all wave modes, including interface waves such as Scholte waves. Numerical results confirm that the vertical component of particle velocity remains continuous across the interface, while the horizontal components and pressure are discontinuous. Moreover, the negative vertical stress at a horizontal seabed equals the hydrostatic pressure immediately above it.

Comparisons with field data from the East China Sea show that although field records exhibit broader bandwidth and more spectral notches, the AECE-simulated data captures the essential waveform characteristics, particularly in the low-frequency band where Scholte waves dominate. Critically, the pressure component simulated by AECE represents true physical pressure, allowing direct comparison with field hydrophone recordings – a significant advantage over traditional methods that often yield mathematical abstractions rather than physically measurable quantities.

The AECE provides a robust and unified framework for simulating complex wave propagation in coupled marine environments, offering a high-quality numerical foundation for subsequent elastic reverse time migration, full waveform inversion, and multicomponent seismic interpretation.

CRediT authorship contribution statement

Peng-Fei Yu: Writing – original draft, Supervision, Methodology, Funding acquisition. **Yong-Tian Zhao:** Writing – review & editing, Software. **Jia-Wei Zhang:** Writing – review & editing, Methodology. **Xiao-Hui Yang:** Supervision, Resources, Project administration. **Chao Zhang:** Writing – review & editing, Supervision.

Declaration of competing interest

The authors declare that they have no known competing financial interests or personal relationships that could have appeared to influence the work reported in this paper.

Acknowledgments

This work was supported by National Natural Science Foundation of China (42074149) and Scientific Research Foundation for High-level Talents of Anhui University of Science and Technology (2025yjrc0001).

Appendix A. 3D AECE in isotropic media

The AECE in 3D isotropic media includes three equations (Yu et al., 2016, 2023): the motion equation

$$\begin{cases} \rho\dfrac{\partial v_x}{\partial t} = \dfrac{\partial\left(\tau_{xx}^{S}-p\right)}{\partial x} + \dfrac{\partial \tau_{xy}^{S}}{\partial y} + \dfrac{\partial \tau_{xz}^{S}}{\partial z} \\ \rho\dfrac{\partial v_y}{\partial t} = \dfrac{\partial \tau_{xy}^{S}}{\partial x} + \dfrac{\partial\left(\tau_{yy}^{S}-p\right)}{\partial y} + \dfrac{\partial \tau_{yz}^{S}}{\partial z} \\ \rho\dfrac{\partial v_z}{\partial t} = \dfrac{\partial \tau_{xz}^{S}}{\partial x} + \dfrac{\partial \tau_{yz}^{S}}{\partial y} + \dfrac{\partial\left(-\left(p+\tau_{xx}^{S}+\tau_{yy}^{S}\right)\right)}{\partial z} \end{cases}, \tag{A-1}$$

the isotropic stress-strain equation

$$\frac{\partial p}{\partial t} = -K\left(\frac{\partial v_x}{\partial x} + \frac{\partial v_y}{\partial y} + \frac{\partial v_z}{\partial z}\right) + h^{\mathrm{P}}, \tag{A-2}$$

and the deviatoric stress-strain equation

$$\begin{cases} \dfrac{\partial \tau_{xx}^{S}}{\partial t} = \dfrac{\partial(\tau_{xx}+p)}{\partial t} = \dfrac{2\mu}{3}\left(2\dfrac{\partial v_x}{\partial x} - \dfrac{\partial v_y}{\partial y} - \dfrac{\partial v_z}{\partial z}\right) \\ \dfrac{\partial \tau_{yy}^{S}}{\partial t} = \dfrac{\partial(\tau_{yy}+p)}{\partial t} = \dfrac{2\mu}{3}\left(2\dfrac{\partial v_y}{\partial y} - \dfrac{\partial v_x}{\partial x} - \dfrac{\partial v_z}{\partial z}\right) \\ \dfrac{\partial \tau_{xz}^{S}}{\partial t} = \mu\left(\dfrac{\partial v_x}{\partial z} + \dfrac{\partial v_z}{\partial x}\right) \\ \dfrac{\partial \tau_{xy}^{S}}{\partial t} = \mu\left(\dfrac{\partial v_x}{\partial y} + \dfrac{\partial v_y}{\partial x}\right) \\ \dfrac{\partial \tau_{yz}^{S}}{\partial t} = \mu\left(\dfrac{\partial v_y}{\partial z} + \dfrac{\partial v_z}{\partial y}\right) \end{cases}. \tag{A-3}$$

$\mathbf{\Phi} = \left(p, \tau_{xx}^{S}, \tau_{yy}^{S}, \tau_{xy}^{S}, \tau_{xz}^{S}, \tau_{yz}^{S}\right)^{\mathrm{T}}$ is a stress vector composed of isotropic stress components and deviatoric stress components. h^{P} represents a P-wave source.

Appendix B. Stress and displacement continuity conditions at the seabed interface

At the ocean bottom fluid-solid coupling interface, the stress tensor and displacement vector need to satisfy certain continuity conditions, as shown in Fig. B-1,

$$\vec{\mathbf{n}}\cdot\mathbf{T} = -p\cdot\vec{\mathbf{n}}, \tag{B-1}$$

$$\mathbf{u}^{\mathrm{f}}(\mathbf{x},t)\cdot\vec{\mathbf{n}} = \mathbf{u}^{\mathrm{s}}(\mathbf{x},t)\cdot\vec{\mathbf{n}}. \tag{B-2}$$

Eqs. (B-1) and (B-2) represent the stress continuity conditions and displacement continuity conditions, respectively. The normal direction of the interface $\vec{\mathbf{n}} = (\cos(\theta_1)\sin(\theta_2),\ \sin(\theta_1)\sin(\theta_2),\ \cos(\theta_2))$. $\mathbf{u}^{\mathrm{f}}(\mathbf{x},t) = \left(u_x^{\mathrm{f}}, u_y^{\mathrm{f}}, u_z^{\mathrm{f}}\right)$ represents the displacement vector in the fluid, and $\mathbf{u}^{\mathrm{s}}(\mathbf{x},t) = \left(u_x^{\mathrm{s}}, u_y^{\mathrm{s}}, u_z^{\mathrm{s}}\right)$ represents the displacement vector in the solid, respectively.

The expanded expression of Eq. (B-1) is:

$$\begin{aligned}
-p\cos(\theta_1)\sin(\theta_2) &= \tau_{xx}\cos(\theta_1)\sin(\theta_2) + \tau_{xy}\sin(\theta_1)\sin(\theta_2) + \tau_{xz}\cos(\theta_2),\\
-p\sin(\theta_1)\sin(\theta_2) &= \tau_{xy}\cos(\theta_1)\sin(\theta_2) + \tau_{yy}\sin(\theta_1)\sin(\theta_2) + \tau_{yz}\cos(\theta_2),\\
-p\cos(\theta_2) &= \tau_{xz}\cos(\theta_1)\sin(\theta_2) + \tau_{yz}\sin(\theta_1)\sin(\theta_2) + \tau_{zz}\cos(\theta_2).
\end{aligned} \tag{B-3}$$

When the fluid-solid coupling interface is horizontal, $\theta_1 = 0°$, $\theta_2 = 0°$, then Eq. (B-1) simplifies to

$$\begin{aligned}
\tau_{xz} &= 0,\\
\tau_{yz} &= 0,\\
\tau_{zz} &= -p.
\end{aligned} \tag{B-4}$$

Eq. (B-2) simplifies to

$$u_z^{\mathrm{f}}(\mathbf{x},t) = u_z^{\mathrm{s}}(\mathbf{x},t). \tag{B-5}$$

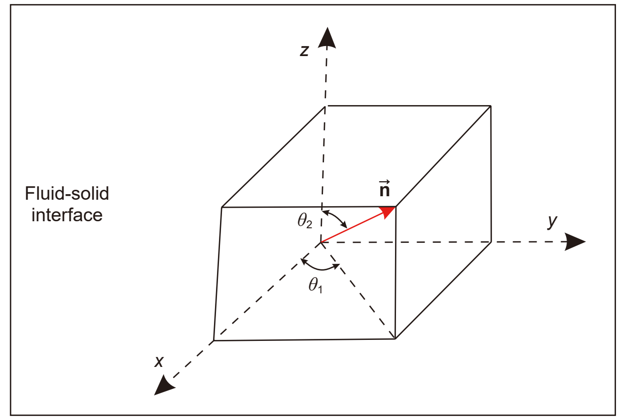

Fig. B-1. The diagram of fluid-solid interface condition.

Appendix C. Reflection/transmission coefficient formulas at the seabed interface

In the 2D case, when a down-going P-wave is incident upon the seafloor interface (Fig. C-1(b)), generates reflected P-waves, transmitted P/S-waves, and Scholte waves, satisfying energy conservation:

$$R_{\mathrm{P^+P^-}} + T_{\mathrm{P^+P^+}} + T_{\mathrm{P^+S^+}} + S = 1, \tag{C-1}$$

$R_{\mathrm{P^+P^-}}, T_{\mathrm{P^+P^+}}, T_{\mathrm{P^+S^+}}, S$ represent the reflection coefficient of P-waves, the transmission coefficient of P-waves, the transmitted coefficient of S-waves, and the Scholte wave coefficient, respectively.

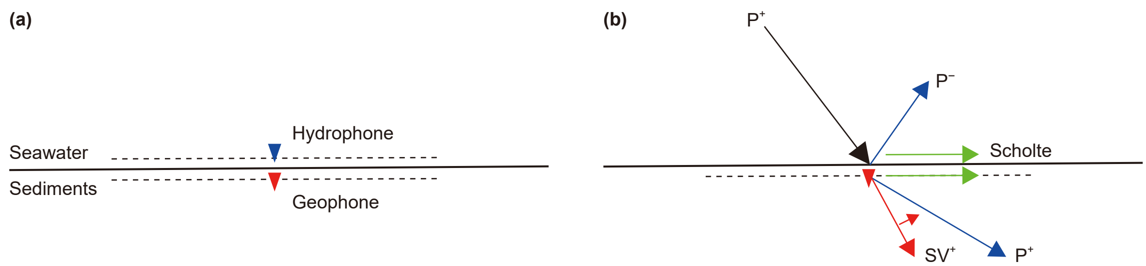

Fig. C-1. Energy partitioning relationships of wavefields at the seafloor interface for a source excited in seawater: (**a**) positions of the hydrophone and geophone at the seafloor; (**b**) case of incident down-going P-wave. Superscripts "+" and "−" denote down-going and up-going wavefields, respectively. Solid long arrows indicate the direction of wavefield propagation.

The energy distribution of Scholte waves at the seafloor interface requires solving the Scholte wave dispersion equation. Based on the Zoeppritz equations, the reflection and transmission coefficients at the seabed interface can be derived (Buckingham, 2005):

$$\begin{cases} R_{\mathrm{P^+P^-}} = \dfrac{\left(1-2p^2\beta^2\right)^2 \rho q_{\mathrm{W}} + 4p^2\beta^4 \rho q_\alpha q_\beta q_{\mathrm{W}} - \rho_{\mathrm{W}} q_\alpha}{\left(1-2p^2\beta^2\right)^2 \rho q_{\mathrm{W}} + 4p^2\beta^4 \rho q_\alpha q_\beta q_{\mathrm{W}} + \rho_{\mathrm{W}} q_\alpha} \\ T_{\mathrm{P^+P^+}} = \dfrac{-4\alpha_{\mathrm{W}}\beta p \rho_{\mathrm{W}} q_\alpha q_{\mathrm{W}}}{\left(1-2p^2\beta^2\right)^2 \rho q_{\mathrm{W}} + 4p^2\beta^4 \rho q_\alpha q_\beta q_{\mathrm{W}} + \rho_{\mathrm{W}} q_\alpha}, \\ T_{\mathrm{P^+S^+}} = \dfrac{2\alpha_{\mathrm{W}}\alpha^{-1}\rho_{\mathrm{W}} q_{\mathrm{W}}\left(1-2p^2\beta^2\right)}{\left(1-2p^2\beta^2\right)^2 \rho q_{\mathrm{W}} + 4p^2\beta^4 \rho q_\alpha q_\beta q_{\mathrm{W}} + \rho_{\mathrm{W}} q_\alpha} \end{cases} \tag{C-2}$$

where α_{W}, ρ_{W} are velocity and density of the water layer, respectively. α, β, ρ represent P-wave velocity, S-wave velocity, and density of the sediments, respectively. p is the horizontal slowness of the incident wavefield, and $q_{\mathrm{W}} = \sqrt{\alpha_{\mathrm{W}}^{-2} - p^2}$, represent vertical slowness in the water layer; $q_\alpha = \sqrt{\alpha^{-2} - p^2}$, represent the vertical slowness for P-waves in the sediments; $q_\beta = \sqrt{\beta^{-2} - p^2}$, represents the vertical slowness for S-waves in the sediments. Based on Eqs. (C-1) and (C-2), the energy coefficient of the Scholte wave at the seabed interface can be obtained.

References

Bader, M., Almquist, M., Dunham, E.M., 2023. Modeling and inversion in acoustic-elastic coupled media using energy-stable summation-by-parts operators. Geophysics 88 (3), T137–T150. https://doi.org/10.1190/GEO2022-0195.1.

Buckingham, M.J., 2005. Compressional and shear wave properties of marine sediments: Comparisons between theory and data. J. Acoust. Soc. Am. 117 (1), 137–152. https://doi.org/10.1121/1.1810231.

Carcione, J.M., Helle, H.B., 2004. The physical and simulation of wave propagation at the ocean bottom. Geophysics 69 (3), 25–39. https://doi.org/10.1190/1.1759469.

Carcione, J.M., Bagaini, C., Ba, J., et al., 2018. Waves at fluid-solid interfaces: Explicit versus implicit formulation of the boundary condition. Geophys. J. Int. 215, 37–48. https://doi.org/10.1093/gji/ggy262.

Chen, Y., Wang, D., 2024. Numerical modeling of scholte wave in acoustic-elastic coupled TTI anisotropic media. Appl. Sci. 14 (18), 8302. https://doi.org/10.3390/app14188302.

Ewing, W.M., Jardetzky, W.S., Press, F., 1957. Elastic Waves in Layered Media. McGraw-Hill, New York.

Greaves, R.J., Stephen, R.A., 2000. Low-grazing-angle momostatic acoustic reverberation from rough and heterogeneous seafloors. J. Acoust. Soc. Am. 108 (3), 1013–1025. https://doi.org/10.1121/1.1288664.

Kugler, S., Bohlen, T., Forbriger, T., et al., 2007. Scholte-wave tomography for shallow-water marine sediments. Geophys. J. Int. 168 (2), 551–570. https://doi.org/10.1111/j.1365-246X.2006.03233.x.

Lecoulant, J., Guennou, C., Guillon, L., et al., 2022. Numerical modeling and observations of seismo-acoustic waves propagating as modes in a fluid-solid wave-guide. J. Acoust. Soc. Am. 151 (5), 3437–3447. https://doi.org/10.1121/10.0010529.

Li, Z.C., Qu, Y.M., 2022. Research progress on seismic imaging technology. Pet. Sci. 19 (1), 128–146. https://doi.org/10.1016/j.petsci.2022.01.015.

Li, Q., Wu, G., Jia, Z., 2023. Full-waveform inversion in acoustic-elastic coupled media with irregular seafloor based on the generalized finite-difference method. Geophysics 88 (2), T83–T100. https://doi.org/10.1190/GEO2022-0408.1.

Li, J., Qu, Y., Li, Y., et al., 2024. Ocean bottom dual-sensor Q-compensated elastic least-squares reverse time migration based on acoustic and separated-viscoelastic coupling equations. Geophysics 89 (3), S155–S173. https://doi.org/10.1190/geo2023-0433.1.

Pramik, B., 2013. Marine vibroseis: shaking up the industry. First Break 31 (11), 67–72. https://doi.org/10.3997/1365-2397.31.11.71796.

Qu, Y., Huang, J., Li, Z., et al., 2015. The application of variable coordinate system forward modeling using cell-based staggered grids in acoustic-elastic coupled medium. Geophys. Prospect. Pet. 54 (5), 582–591. https://doi.org/10.3969/j.issn.1000-1441.2015.05.011 (in Chinese).

Qu, Y., Li, J., Li, Y., et al., 2023. Joint acoustic and decoupled-elastic least squares reverse time migration for simultaneously using water-land dual-detector data. IEEE Trans. Geosci. Rem. Sens. 61, 1–11. https://doi.org/10.1109/TGRS.2023.3270930.

Scholte, J.G., 1947. The range of existence of Rayleigh and Stoneley waves. Geophys. J. Int. 5, 120–126. https://doi.org/10.1111/j.1365-246X.1947.tb00347.x.

Sun, Y.C., Zhang, W., Ren, H.X., et al., 2021. 3D Seismic-wave modeling with a topographic fluid-solid interface at the sea bottom by the curvilinear-grid finite-difference method. Bull. Seismol. Soc. Am. 111 (5), 2753–2779. https://doi.org/10.1785/0120200363.

Tang, J.X., Zhou, H., Jiang, C.T., et al., 2022. A perfectly matched layer technique applied to lattice spring model in seismic wavefield forward modeling for Poisson's solids. Bull. Seismol. Soc. Am. 112 (2), 608–621. https://doi.org/10.1785/0120210166.

Virieux, J., 1986. P-SV wave propagation in heterogeneous media: velocity-stress finite-difference method. Geophysics 51 (4), 889–901. https://doi.org/10.1190/1.1441605.

Wang, Y., Li, Z., Geng, J., et al., 2020. Seismic imaging of S-wave structures of shallow sediments in the East China Sea using OBN multicomponent Scholte-wave data. Geophysics 85 (6), N87–N104. https://doi.org/10.1190/GEO2019-0639.1.

Wang, H., Xiang, J., Shi, Y., 2024a. Basic logic and key methods of OBN seismic data imaging processing. Geophys. Prospect. Pet. 63 (1), 12–29. https://doi.org/10.12431/issn.1000-1441.2024.63.01.002 (in Chinese).

Wang, T., Liu, X., Cheng, J., 2024b. Wave modes of multicomponent OBC/OBN data under typical water depth and bottom medium conditions. Geophys. Prospect. Pet. 63 (1), 45–60. https://doi.org/10.12431/issn.1000-1441.2024.63.01.004 (in Chinese).

Xia, M., Zhou, H., Jiang, C., et al., 2024. Wave propagation across fluid-solid interfaces with LBM-LSM coupling schemes. Pet. Sci. 21 (5), 3125–3141. https://doi.org/10.1016/j.petsci.2024.05.010.

Xie, Y., Zhou, B., Zhou, J., et al., 2017. Orthorhombic full-waveform inversion for imaging the Luda field using wide-azimuth ocean-bottom-cable data. Lead. Edge 36 (1), 75–80. https://doi.org/10.1190/tle36010075.1.

Xie, Y., Ye, Y., Huang, X., et al., 2024. Advancements and new frontiers in offshore seismic exploration technology. J. Earth Sci. 35, 1749–1757. https://doi.org/10.1007/s12583-024-0075-3.

Xu, X., Wan, Y.G., Li, Z.Y., et al., 2022. Scholte wave dispersion and particle motion mode in ocean and ocean crust. Appl. Geophys. 19 (1), 132–142. https://doi.org/10.1007/s11770-022-0931-9.

Yu, P., Geng, J., 2019. Acoustic-elastic coupled equations in vertical transverse isotropic media for pseudo-acoustic-wave reverse time migration of ocean-bottom 4C seismic data. Geophysics 84 (4), S317–S327. https://doi.org/10.1190/GEO2018-0295.1.

Yu, P., Geng, J., Li, X., et al., 2016. Acoustic-elastic coupled equation for ocean bottom seismic data elastic reverse-time migration. Geophysics 81 (5), S333–S345. https://doi.org/10.1190/GEO2015-0535.1.

Yu, P., Chu, M., Xu, Y., et al., 2023. Joint elastic reverse time migration of towed streamer and sparse ocean-bottom seismic node hybrid data. Geophysics 88 (1), S47–S57. https://doi.org/10.1190/GEO2021-0333.1.
Yu, P., Jiang, J., Geng, J., et al., 2024. Shear wave velocity inversion of marine sediments using deep-water OBS Scholte-wave data. Appl. Geophys. 21, 13–30. https://doi.org/10.1007/s11770-024-1073-z.
Zhang, J., 2004. Wave propagation across fluid-solid interfaces: A grid method approach. Geophys. J. Int. 159 (1), 240–252. https://doi.org/10.1111/j.1365-246X.2004.02372.x.
Zhang, B., Wu, G., Shan, J., et al., 2023. Simulation of a wavefield in VTI media adopting an acoustic-elastic coupled equation. In: 84th EAGE Annual Conference & Exhibition. https://doi.org/10.3997/2214-4609.202310913.
Zhen, S., Xing, J., Jiang, X., 2023. Seabed physical parameter research based on active-source OBS data in the Chukchi sea shelf of the Arctic. J. Ocean Univ. China 22, 675–682. https://doi.org/10.1007/s11802-023-5311-4.
Zou, Q., Huang, J., Yong, P., et al., 2020. 3D elastic waveform modeling with an optimized equivalent staggered-grid finite-difference method. Pet. Sci. 17 (4), 967–989. https://doi.org/10.1007/s12182-020-00477-3.